High-Resolution 5G Active Antenna Beam Pattern Measurement Using UAVs

D. M. K. K. Venkateswara Rao, Sumit Kumar, Hamed Habibi, Jorge Querol,
Symeon Chatzinotas, Holger Voos
Interdisciplinary Centre for Security, Reliability and Trust, *University of Luxembourg*
Luxembourg, Luxembourg
{mohan.dasari, sumit.kumar, hamed.habibi, jorge.querol, symeon.chatzinotas, holger.voos}@uni.lu

***Abstract*— This paper presents a measurement methodology for obtaining a high-resolution beam pattern of 5G active antenna systems (AASs) using Unmanned Aerial Vehicles (UAVs). Beam pattern measurements are typically conducted in an anechoic chamber by placing the active antenna at the center and radiation pattern is measured at various angles. This approach is limited by the spatial constraints of the chamber and is time-consuming for obtaining high-resolution measurements. To address this problem, UAVs equipped with measurement sensors are proposed to fly around the antenna and do the measurement campaign. The beam pattern measurement campaign problem is formulated into a UAV path planning problem. Horizontal circular arcs at various elevation angles are defined on a sphere centered at the antenna and connected at their ends alternatively to define a reference path and transcribe it into a reference trajectory for the UAV. A chattering-free super-twisting controller is designed to accurately track this trajectory against unknown matched disturbances and model uncertainties. The proposed methodology is validated by an indoor experiment with a horn antenna set up to operate in the frequency range of a 5G AAS and create a stationary beam. A universal software radio peripheral is mounted on a UAV and programmed to measure the received signal strength indicator in real time and a high-resolution beam pattern is satisfactorily captured.**

***Index Terms*— 5G, Unmanned Aerial Vehicles, Antenna Pattern Measurement, Super-Twisting Control**

Supplementary Material

Video: https://youtu.be/0MLEIXxxV-Q

I. Introduction

Unmanned Aerial Vehicles (UAVs) are increasingly being used for a wide range of applications, including terrain mapping [1], [2], monitoring [3], precision agriculture [4], search and rescue [5], surveillance [6], flood detection [7], etc. There is a significant interest in expanding the applications for urban operations, like airborne delivery [8], traffic monitoring [9], crowd surveillance [10], infrastructure inspection [11], air mobility [12], etc. However, several challenges arise in terms of safe operations such as collision avoidance, loss of GPS signal, electromagnetic interference, etc [13]. Some of the associated risks can be mitigated by having robust communication security [14] and accurate positioning [15]. With the recent advances in cellular communication technology, 5G is being considered to provide aerial coverage and navigation [16] for UAVs.

One of the most important features of 5G is its Active Antenna System (AAS), which utilizes multiple antennas and beamforming to enhance signal quality and network capacity. By dynamically adjusting radio wave direction, AAS minimizes interference and extends coverage. Measuring the beam pattern of 5G AAS is crucial for assessing antenna performance in terms of signal coverage, directionality, and beamforming accuracy. It enables operators to verify if antennas meet specifications and optimize coverage and capacity. Analysis of beam pattern data helps identify interference sources, aiding in mitigation strategies and improving network quality. Further, compliance with regulatory standards is ensured through comparing measured patterns with performance criteria.

The measurement of the beam pattern can be performed using a variety of techniques, such as far-field measurement, near-field measurement, and electromagnetic simulation. Far-field measurements are typically conducted in an anechoic chamber, where the active antenna under test is placed at the center of the chamber and the radiation pattern is measured at various angles. Near-field measurements, on the other hand, are typically performed using a probe and a near-field scanner, which are used to measure the electric and magnetic fields in the vicinity of the antenna. On the other hand, sophisticated software could be used to model the antenna geometry, materials, and environment where one can also simulate the radiation patterns. These measurement techniques are important for evaluating the performance of 5G active antennas and ensuring that they meet the desired specifications for 5G communication.

Nonetheless, measuring the beam pattern of 5G AAS poses challenges due to complex antenna configurations and sophisticated beamforming capabilities. Higher frequency

This work is funded by the Department of Media, Telecommunications and Digital Policy (SMC) of the Government of the Gran Duchy of Luxembourg under the project reference SMC/CFP-2019/010/IRANATA, "Interference and RAdiation in Network PlAnning of 5G AcTive Antenna Systems."

bands in 5G exacerbate measurement difficulties, requiring specialized equipment to mitigate diffraction effects. The dynamic nature of AAS antennas, adjusting beams in real-time, complicates measurement accuracy. Multipath propagation in real-world environments distorts measured patterns, impacting performance characterization. Environmental factors such as reflections and obstructions introduce errors in measurements. Calibration and validation of measurement equipment are crucial to ensure accuracy amidst potential errors and inconsistencies. However, far-field measurements carried out in indoor anechoic chambers have spatial limitations and are time-consuming due to the moving of measurement apparatus.

Despite these challenges, UAVs can be used to measure beam patterns instead of far-field measurements in anechoic chambers, which impose spatial limits. Although authorization is required to fly UAVs outdoors [17], their ability to quickly and accurately position the measurement equipment at varying locations decreases the measurement campaign time. There are several applications of UAVs being used for measuring 5G antenna performance in the literature. In [18], UAVs are used to measure the Reference Signal Received Power (RSRP) of a single eNodeB in LTE band 20 to carry out spatial analysis of the fading effect. In [19], UAVs are used to characterize 3-D wireless propagation of 27 and 38 GHz frequency millimeter waves(mmWaves). A UAV-based channel measurement system with spectrum analyzer was created in [20] that can be used to carry out interference studies and link budget calculation. An air-to-ground(AG) measurement campaign was carried out in [21] to model path loss exponent and investigate small-scale fading for different altitudes. Similar works were carried out in [22]–[24] for AG channel characterization. A UAV-based in-situ measurement and diagnostic system was developed in [25] for mmWave frequency mobile network antennas. In [26], UAVs were used to measure Signal-to-Interference-Plus-Noise Ratio (SINR) and RSRP at different heights in remote and urban areas, with and without 4G services, respectively, for testing the viability of UAVs as flying relays or base stations. In [27], field trials were carried out using UAVs in a suburban area to measure different 4G/5G performance metrics, downlink and uplink throughputs, and study handover events for meeting connectivity requirements and show coexistence with terrestrial users.

In this paper, a novel UAV-based measurement methodology is proposed that can be used to measure the beam pattern of a 5G AAS. It is our goal to facilitate a high-resolution beam pattern measurement quickly, accurately, and automatically using UAVs. An indoor setup is created with a signal generator powering a horn antenna to create a stationary beam pattern similar to that generated by a 5G AAS. To the best of our knowledge, we extended the application of UAVs for the beam pattern measurement of an antenna for the first time. A Software Defined Radio (SDR) device is programmed to measure and low-pass filter Received Signal Strength Indicator (RSSI) in real time. The SDR device is mounted on a quadrotor UAV that can hover and fly at extremely low velocities. As beam pattern measurements are carried out at points located at various angles and equal distances from the antenna, a spherical section is defined in the field of view of the antenna for the UAV to traverse and carry out a measurement campaign. Horizontal arcs separated by equal elevation intervals are defined on this spherical surface. These are connected at their ends alternatively to form a snake-like path for the UAV. By choosing a small and constant angular velocity, the path is transcribed into a reference trajectory. The addition of an SDR device and onboard computer adds significant uncertainty to the model and leads to poor tracking performance by the default controller on the autopilot. As tracking performance affects measurement accuracy, the need for a robust and accurate controller is crucial. Owing to the robustness in addressing matched uncertainties and disturbances, a Super-Twisting Controller (STC) [28], [29] is designed to track the reference trajectory accurately. Finally, an indoor experiment is carried out to show the viability of the proposed approach.

The rest of the paper is organized as follows. Sec. II presents the details of antenna setup for beamforming, real-time measurement of RSSI signal levels, UAV and indoor lab setup, path and trajectory planning for carrying out high-resolution measurement campaign, and the design of STC. Results of the experiment are presented and discussed in Sec. III. The paper ends with concluding remarks in Sec. IV.

II. Measurement Methodology

A. Experiment Setup

The focus of our investigation is on the radiated far-field region of the active antenna. We conducted experiments using an emulated gNB setup, featuring a unidirectional connection where the gNB directs a downlink beam towards a static UE. Utilizing a commercial 5G vector signal generator [30] capable of generating standard-compliant 5G-NR Time Division Duplex (TDD) waveforms, we simulated the gNB. However, our setup lacks the capability for beam sweeping, necessitating an alternative approach. To emulate an active-antenna gNB system creating a dedicated beam towards the UE, we employed a highly directive horn antenna [31], albeit not an exact representation, closely mimicking beam correspondence. Besides, in our experiments, since a "REAL" UE is not required to establish beam-correspondence [32] with the gNB, but the gNB (and the beam generated by the connected horn antenna) is in our full control, we point the beam in the direction of maximum unobstructed length inside our lab. During the beam pattern measurement of a 5G AAS from a commercial gNB outdoors, the beam is maintained constant towards the UE during downlink traffic. Our experiment set-up, which is discussed above, is closely aligned with it that is the horn antenna maintains a continuous focused beam towards the UE. The transmission frequency for experiments is 3.775 GHz under a license

obtained from the Institut Luxembourgeois de Régulation (ILR) for experimental purposes.

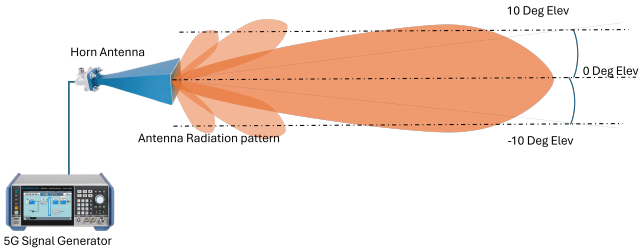

Fig. 1. Illustration of signal generator and horn antenna setup used for the experiments.

To measure the strength of the transmitted signal, we required a lightweight power sensor that can be tuned to the frequency of operation, i.e., 3.775 GHz. We opted for Ettus USRP B205mini-i [33] which is an SDR-based solution. It can be tuned from 70 MHz to 6 GHz and can sample at a maximum rate of 56MHz. The USRP is connected to Raspberry Pi which also hosts a Universal Hardware Driver (Ettus UHD) [34], a driver that is required to operate the chosen USRP. To assess the power of the transmitted beam, we have chosen RSSI as our metric since it is not required to decode the signal to measure this metric. This is in contrast to other parameters of 5G such as RSRP which requires decoding the 5G preamble first [35]. To read the values of RSSI, we came up with our own C++ code which calls the UHD C++ API to read the RSSI values.

For N number of complex samples which are collected by the ADC (Analog to Digital Converter), the RSSI is computed as

$$\text{RSSI}(i) = \frac{1}{N}\sum_{k=1}^{N} |x_k(i)|^2 \tag{1}$$

where $x_k(i)$ represents the k^{th} complex sample for time step i. Further, the RSSI values are converted into dB.

The high-frequency noisy raw RSSI measurements are passed through a low-pass filter as

$$\text{RSSI}_{LPF}(i+1) = (1-\tau)\text{RSSI}_{LPF}(i) + \tau\text{RSSI}(i) \tag{2}$$

where τ is the time constant.

Once the SDR + Raspberry Pi set is mounted on the UAV, it starts taking RSSI measurements with 1 reading per second. It sends the RSSI values via a UDP port (over WiFi) to another static machine on the ground which is depicted in Figure-3. Here the RSSI values are collected from the pre-assigned UDP port via a MATLAB program which also performs low-pass filtering over the incoming RSSI values to filter out any sudden jump.

B. UAV and Indoor Lab Setup

The UAV used for the experiments in this paper is a customized QAV250 model quadrotor as shown in Fig. 2. The onboard components of the UAV, indoor positioning system, and network architecture used for communication are illustrated in Fig. 3. The UAV is equipped with a Pixhwak CUAV V5 Nano autopilot running the PX4 operating system. A Raspberry Pi Model B, running Ubuntu server 20.04 is used as an onboard computer. This is interfaced with both autopilot and USRP B205mini-i, which measures the RSSI signals. For localization, we use an Optitrack system comprising 12 infrared cameras fixed at a height of around 5 m and a high-performance desktop computer running Motive software. The Optitrack system uses infrared cameras to detect the circular reflective markers attached to the UAV and determines its position and orientation relative to a predefined Front-Left-Up inertial coordinate system at a frequency of 120 Hz. The onboard computer running rosmaster receives the estimated position and orientation of the UAV from the Motive software over WiFi and relays it to the autopilot via mavros. The autopilot fuses this information with its angular rate and acceleration measurements to estimate the full state of the UAV and relays it back to mavros node. The ground control station runs Matlab, which subscribes to mavros node for UAV state, acceleration, and angular rate and implements the STC. It also receives raw RSSI measurements from the USRP via UDP port and low-pass filters them to remove noise. The computed control inputs, $i.e.$, normalized thrust, orientation, and angular rates are commanded to the UAV via mavros, which relays them to the autopilot. The low-level controller in the autopilot determines and commands the motor control inputs.

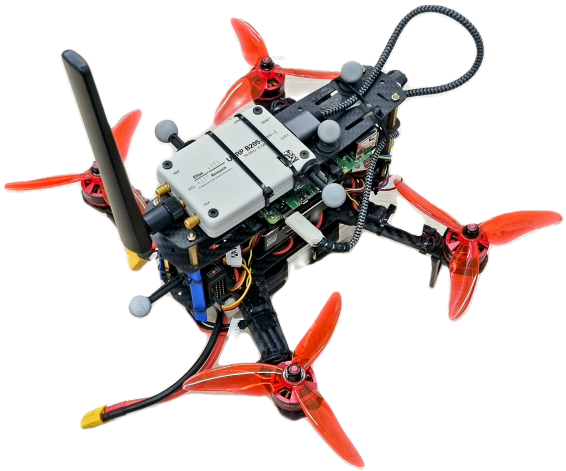

Fig. 2. UAV equipped with USRP and Raspberry Pi used for the experiments.

C. UAV Path and Trajectory Planning

Antenna pattern is usually measured by taking signal measurements at points located equidistant from the antenna. Therefore, the locus of the measurement points would be a spherical surface with the antenna's position as its origin. The horn antenna system considered in this paper mimics

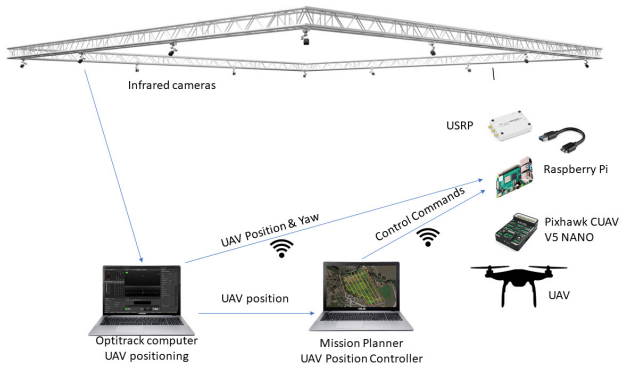

Fig. 3. Illustration of the UAV, positioning, and control network setup in the lab.

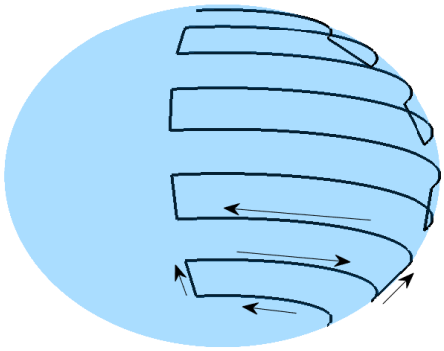

Fig. 4. Illustration of the UAV path on a circular sphere.

the beamforming capability of a 5G AAS. There will be a directed beam in the desired direction and to capture it, measurements need not be carried out all over the area of the spherical surface. Only a section of the surface with chosen elevation and azimuth angle ranges is of interest.

To define a path for the UAV to traverse this section, similar to a coverage mapping problem, let us consider a sphere of radius R centered at the antenna. Also, consider Cartesian and spherical coordinate systems with the same origin. Assuming that the beam's direction is parallel to the ground, define x-axis in the direction of the beam, and z-axis in the upward direction and perpendicular to the ground. y-axis is chosen to complete the right-hand coordinate system. The Cartesian and spherical coordinates of a point are related to each other as

$$x = R\cos\Theta\cos\Psi \tag{3a}$$
$$y = R\cos\Theta\sin\Psi \tag{3b}$$
$$z = R\sin\Theta \tag{3c}$$

where x, y, and z are the Cartesian coordinates; Ψ is the azimuth; and Θ is the elevation.

Define ranges for azimuth and elevation angles

$$\Psi \in [\Psi_{min}, \Psi_{max}] \tag{4a}$$
$$\Theta \in [\Theta_{min}, \Theta_{max}] \tag{4b}$$

For a fixed elevation angle, Θ_d, the section will reduce to a circular arc of constant height. The coordinates of a point $[x_d, y_d, z_d]^T$ on the arc are related to azimuth angle as

$$x_d = R\cos\Theta_d\cos\Psi_d \tag{5a}$$
$$y_d = R\cos\Theta_d\sin\Psi_d \tag{5b}$$
$$z_d = R\sin\Theta_d \tag{5c}$$

If different elevation angles are chosen within their range, a few circular arcs can be defined. These arcs are connected at the ends alternatively to form a snake-like pattern as illustrated in Fig. 4. The resulting curve is defined as the UAV path for the antenna pattern measurement experiment.

The reference trajectory for each arc, $[x_d(t), y_d(t), z_d(t)]^T$, is a point moving at constant angular velocity $\omega(t)$, defined as

$$x_d(t) = R\cos\Theta_d(t)\cos(\Psi_d(t))) \tag{6a}$$
$$y_d(t) = R\cos\Theta_d(t)\sin(\Psi_d(t))) \tag{6b}$$
$$z_d(t) = R\sin\Theta_d(t) \tag{6c}$$
$$\Psi_d(t) = \int_0^t \omega(t)dt \tag{6d}$$

where $\Psi_d(t)$ is the phase angle. When the UAV reaches the end of the arc, the reference trajectory is modified by increasing the elevation angle and changing the sign of the angular velocity for the UAV to move along the next arc in the opposite direction.

D. Controller Design

The six-degrees-of-freedom autonomous form of nonlinear equations of motion [36] of the UAV are given as

$$\begin{bmatrix}\dot{x}(t)\\ \dot{y}(t)\\ \dot{z}(t)\end{bmatrix} = \begin{bmatrix}u(t)\\ v(t)\\ w(t)\end{bmatrix} \tag{7}$$

$$\begin{bmatrix}\dot{u}(t)\\ \dot{v}(t)\\ \dot{w}(t)\end{bmatrix} = \frac{1}{m}R_b^e\begin{bmatrix}0\\ 0\\ T(t)\end{bmatrix} - \begin{bmatrix}D_x\\ D_y\\ g\end{bmatrix} \tag{8}$$

$$\begin{bmatrix}\dot{\phi}(t)\\ \dot{\theta}(t)\\ \dot{\psi}(t)\end{bmatrix} = \begin{bmatrix}1 & \sin\phi(t)\tan\theta(t) & \cos\phi(t)\tan\theta(t)\\ 0 & \cos\phi(t) & -\sin\phi(t)\\ 0 & \sin\phi(t)\sec\theta(t) & \cos\phi(t)\sec\theta(t)\end{bmatrix}\begin{bmatrix}p(t)\\ q(t)\\ r(t)\end{bmatrix} \tag{9}$$

$$\begin{bmatrix}\dot{p}(t)\\ \dot{q}(t)\\ \dot{r}(t)\end{bmatrix} = \begin{bmatrix}((I_{yy}-I_{zz})q(t)r(t)+\tau_x(t))/I_{xx}\\ ((I_{zz}-I_{xx})p(t)r(t)+\tau_y(t))/I_{yy}\\ ((I_{xx}-I_{yy})p(t)q(t)+\tau_z(t))/I_{zz}\end{bmatrix} \tag{10}$$

where $[x(t), y(t), z(t)]^T$ and $[u(t), v(t), w(t)]^T$ are position and velocity variables, respectively, in inertial frame-of-reference; m is mass of the UAV; $T(t)$ is the thrust along z-axis in body frame-of-reference; D_x and D_y are disturbances; $[\phi(t), \theta(t), \psi(t)]^T$ are roll, pitch, and yaw angles; $[p(t), q(t), r(t)]^T$ are roll, pitch, and yaw rates in body frame-of-reference; $[\tau_x(t), \tau_y(t), \tau_z(t)]^T$ are torques in body frame-of-reference; I_{xx}, I_{yy}, and I_{zz} are inertia parameters; R_b^e is the transformation matrix to transfer a vector from body to inertial frame-of-reference given as

$$R_b^e = \begin{bmatrix} C\theta C\psi & S\phi S\theta C\psi - C\phi S\psi & C\phi S\theta C\psi + S\phi S\psi \\ C\theta S\psi & S\phi S\theta S\psi + C\phi C\psi & C\phi S\theta S\psi - S\phi C\psi \\ -S\theta & S\phi C\theta & C\phi C\theta \end{bmatrix} \tag{11}$$

in which C and S stand for cos and sin, respectively.

Let $[x_d(t), y_d(t), z_d(t)]^T$ and $[u_d(t), v_d(t), w_d(t)]^T$ be the desired position and velocity of the UAV. Define sliding functions $s_x(t)$, $s_y(t)$, and $s_z(t)$ as

$$s_x(t) = (u(t) - u_d(t)) + \lambda_x(x(t) - x_d(t)) \tag{12a}$$
$$s_y(t) = (v(t) - v_d(t)) + \lambda_y(y(t) - y_d(t)) \tag{12b}$$
$$s_z(t) = (w(t) - w_d(t)) + \lambda_z(z(t) - z_d(t)) \tag{12c}$$

The dynamics of a sliding variable $s_i(t)$ in super-twisting form is given as

$$\dot{s}_{i_1}(t) = -\alpha_i \textbf{sign}(s_{i_1}(t))|s_{i_1}(t)|^{1/2} + s_{i_2}(t) \tag{13a}$$
$$\dot{s}_{i_2}(t) = -\beta_i \textbf{sign}(s_{i_1}(t)) + \Delta_i(t) \tag{13b}$$

where $i \in [x, y, z]$; $\Delta_i(t)$ is the time-derivative of unknown disturbance; and α_i and β_i are positive constants and are chosen as follows for finite-time convergence of sliding functions to zero [28]

$$\alpha_i > 1.5\sqrt{\max(|\Delta_i(t)|)} \tag{14a}$$
$$\beta_i > \max(|\Delta_i(t)|) \tag{14b}$$

To avoid chattering, the **sign** function is approximated as

$$\textbf{sign}(s) = \frac{s}{|s| + \epsilon} \tag{15}$$

where ϵ is a small positive constant.

This yields a control law for acceleration inputs along each axis in the inertial frame as

$$a_{x_c}(t) = \ddot{x}_d(t) - \lambda_x(\dot{x}(t) - \dot{x}_d(t)) + \dot{s}_{x_1}(t) \tag{16}$$
$$a_{y_c}(t) = \ddot{y}_d(t) - \lambda_y(\dot{y}(t) - \dot{y}_d(t)) + \dot{s}_{y_1}(t) \tag{17}$$
$$a_{z_c}(t) = \ddot{z}_d(t) - \lambda_z(\dot{z}(t) - \dot{z}_d(t)) + \dot{s}_{z_1}(t) + g \tag{18}$$

where $\ddot{x}_d(t)$, $\ddot{y}_d(t)$, and $\ddot{z}_d(t)$ are second-order derivatives of the reference trajectory; $\dot{s}_{x_1}(t)$, $\dot{s}_{x_1}(t)$, and $\dot{s}_{x_1}(t)$ are evaluated based on the right-hand side term of Eqn. (13).

The total thrust acceleration input $T_c(t)$ for the UAV that is distributed to all the motors is determined as

$$T_c(t) = \sqrt{a_{x_c}(t)^2 + a_{y_c}(t)^2 + a_{z_c}(t)^2} \tag{19}$$

The acceleration inputs are transformed into desired orientations as

$$\phi_c(t) = \sin^{-1}\left(\frac{-a_{x_c}(t)\sin(\psi_d(t)) + a_{y_c}(t)\cos(\psi_c(t))}{T_c(t)}\right) \tag{20a}$$

$$\theta_c(t) = \sin^{-1}\left(\frac{a_{x_c}(t)\cos(\psi_d(t)) + a_{y_c}(t)\sin(\psi_c(t))}{T_c(t)\cos\phi_c(t)}\right) \tag{20b}$$

where $\phi_c(t)$, $\theta_c(t)$, and $\psi_c(t)$ are desired roll, pitch, and yaw angles.

Finally, the desired angular rates are determined as

$$\begin{bmatrix} p_c(t) \\ q_c(t) \\ r_c(t) \end{bmatrix} = -\lambda_\omega M \begin{bmatrix} \phi(t) - \phi_c(t) \\ \theta(t) - \theta_c(t) \\ \psi(t) - \psi_c(t) \end{bmatrix} \tag{21}$$

where

$$M = \begin{bmatrix} 1 & 0 & -\sin\theta(t) \\ 0 & \cos\phi(t) & \sin\phi(t)\cos\theta(t) \\ 0 & -\sin\phi(t) & \cos\phi(t)\cos\theta(t) \end{bmatrix} \tag{22}$$

Remark 1: It should be noted that the PX4 autopilot used in the experiments accepts only normalized thrust, Euler angles (20), and angular rates (21) as control inputs. To transform the computed control inputs acceptable to the autopilot, the thrust acceleration is normalized as

$$T_{n_c}(t) = T_c(t)\frac{T_{ref}}{g} \tag{23}$$

where $T_{n_c}(t)$ is the normalized thrust and T_{ref} is the reference normalized thrust when the UAV is hovering.

III. Experiments and Results

Antenna pattern measurements are carried out indoors using the lab setup and methodology presented in Sec. II. The horn antenna is placed at the center of one side of the arena and at a height of 0.75 m pointing toward the center of the arena. The signal generator is placed outside of the arena and powers the antenna through a SMA cable. The frequency and power levels of the antenna are set at 3.775 GHz and -10 dBm, respectively.

A spherical surface section of radius 2 m, elevation and azimuth angle ranges, $[-20°, 50°]$ and $[-60°, 60°]$, respectively, is defined inside the arena with origin at the center of the end plane the antenna. Elevation angles below -20° are not considered due to spatial constraints caused by the ground. The UAV path illustrated in Fig. 4 is defined for the chosen spherical surface section, with horizontal arcs separated by 10° elevation angle intervals. The reference trajectory for each horizontal arc is defined using Eqn. (6) with an initial phase angle of -60° and constant angular velocity of 1.33 deg/s. The angular velocity is chosen so low to fly at low velocities and achieve high angular resolution in the azimuthal direction. The elevation angle is increased by 10° and the sign of the angular velocity is changed every time the UAV reaches the end of an arc. These changes are

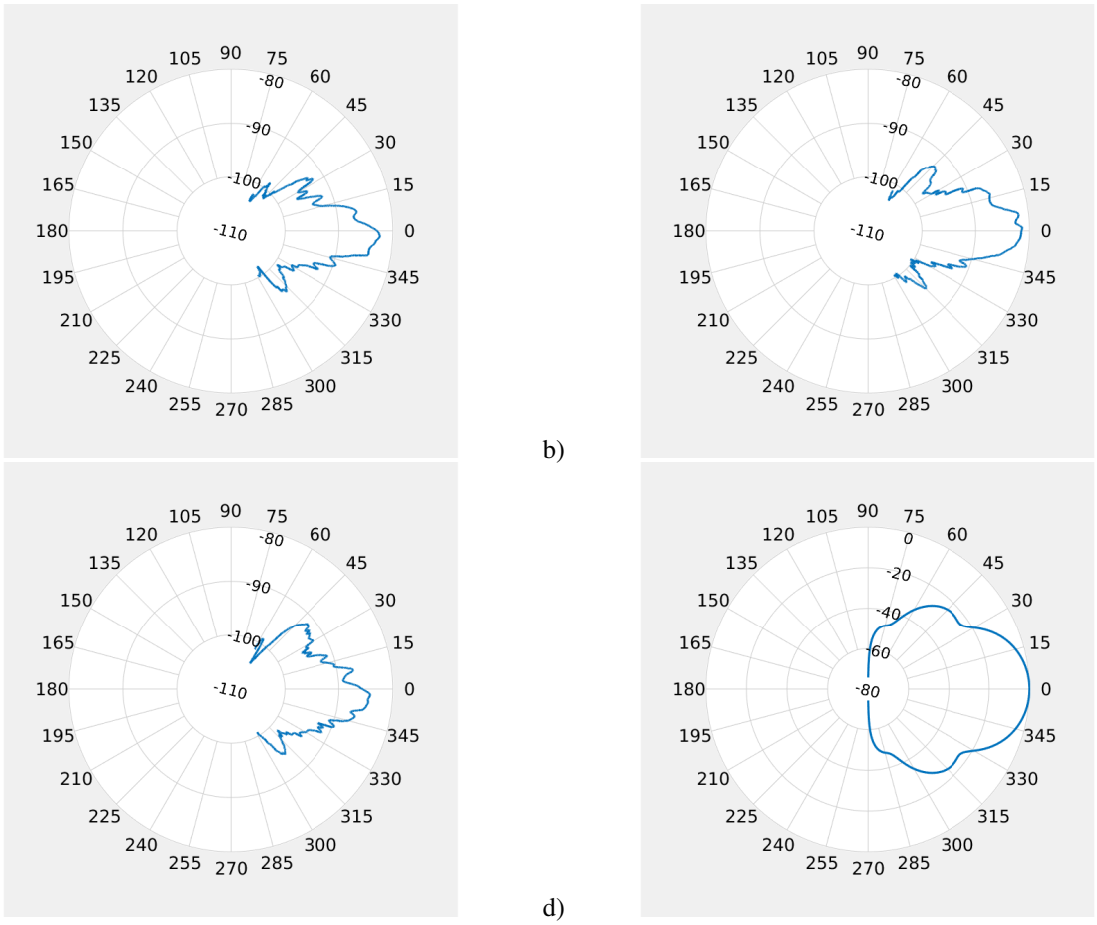

Fig. 5. Polar pattern plots of horn antenna for different elevation angles: a) $\Theta_d = -10°$, b) $\Theta_d = 0°$, and c) $\Theta_d = 10°$, d) Reference polar plot of horn antenna WR229 with 20dBi gain.

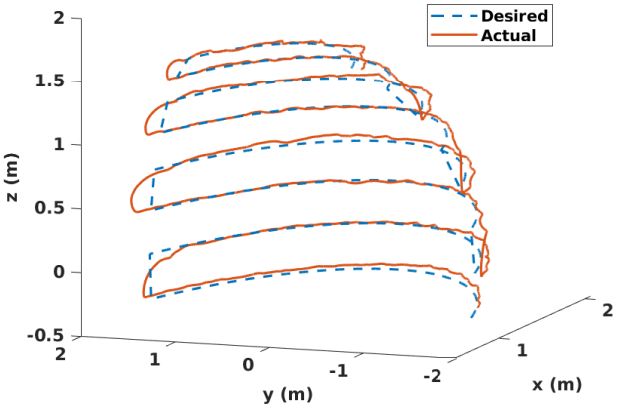

Fig. 6. Desired and actual paths of the UAV.

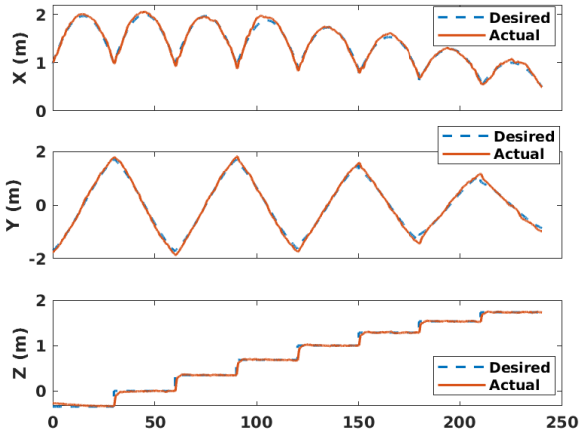

Fig. 7. Time histories of desired and actual UAV trajectories.

continued until the maximum elevation angle is reached. The desired yaw angle of the UAV is chosen to be equal to the phase angle, *i.e.*, $\psi_c(t) = \Psi_d(t)$.

Once the reference trajectory is specified, the parameters of the controller are chosen. The gains in the sliding functions defined in Eqn. (12) are chosen as $\lambda_x = 1$, $\lambda_y = 1$, and $\lambda_z = 4$. The parameters in the super-twisting dynamics given in Eqn. (13) are defined as $\alpha_x = 1.2238$, $\alpha_y = 1.2238$,

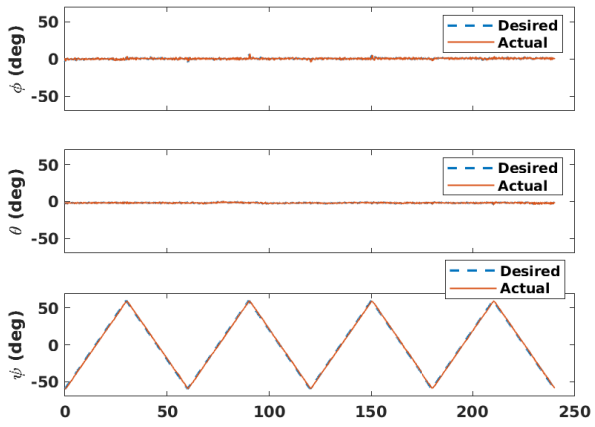

Fig. 8. Time histories of desired and actual Euler angles.

$\alpha_z = 1.7307$, $\beta_x = 0.0284$, $\beta_y = 0.0284$, and $\beta_z = 0.0568$. The constant in Eqn. (15) is chosen as $\epsilon = 0.1$. The parameter λ_ω in Eqn. (21) is defined as $\lambda_\omega = 1$. A hovering maneuver is performed using the default controller available in the PX4 autopilot to experimentally determine the reference normalized thrust in Eqn. (23) as $T_{ref} = 0.38$.

Before starting the antenna pattern measurement campaign, the UAV is commanded to stabilize at the initial point of the desired trajectory for a duration of 15 s so that sliding is reached and the transient motion of the UAV doesn't affect the measurements. Once the UAV is stabilized, the measurement campaign is initiated and the controller is implemented for the UAV to track the reference horizontal arc trajectories. The high-frequency noisy raw RSSI measurements are low-pass filtered and recorded for post-processing.

The sampling rate of ADC in our experiments is 10MHz. This is larger than the bandwidth of interest which is 5MHz in our case. The time constant, τ, of the low-pass filter in Eqn. (2) is chosen as 0.01. The polar pattern plots of the horn antenna for elevation angles $-10°, 0°$, and $10°$ are presented in Fig. 5. Besides a reference polar plot of the horn antenna (WR-229) is shown in (d) for comparison. Please note that (d) has been simulated using antenna dimension as there is no reference pattern available from the manufacturer. Fig. 5(b) corresponds to the RSSI plot at an elevation angle of $0°$ and captures the maximum radiated on the antenna boresight. The width of the main lobe is approximately $60°$ where the RSSI drops to approximately 19 dB. However, in the reference plot (d), the main lobe width is $66°$ where the RSSI drops by approximately 24 dB. Although we see a difference, nonetheless, the main lobe pattern is correctly captured. The reason for such a difference could be mitigated by performing several iterations and averaging the results. The rest two plots in (a) and (c) capture RSSI in a horizontal plane (see Fig.1 at an elevation of $-10°$, and $10°$, hence capture less RSSI compared to the case of (b). This is also evident from the reduced peak power of the main lobe in (a) and (c). Besides, the plots in (a), (b), and (c) successfully capture the side lobes of radiation.

As the tracking accuracy of the UAV affects the beam pattern measurements, reference and actual trajectories are also presented to validate the performance of the designed STC. The desired and actual paths of the UAV are presented in Fig. 6. The time histories of desired and actual trajectories and Euler angles are presented in Fig. 7 and Fig. 8, respectively. It can be seen in Fig. 6 that the UAV has converged to the reference trajectory and followed the reference path very accurately except during the transitions from one arc to another. Along the x, y, and z directions, the maximum absolute errors are 0.16 m, 0.30 m, and 0.07 m, respectively and the root mean square (RMS) errors are 0.04 m, 0.08 m, and 0.04 m, respectively. The maximum absolute and RMS errors in roll, pitch, and yaw are $5.5°$, $3.0°$, and $2.3°$ and $0.94°$, $0.57°$, and $1.19°$, respectively. It can be seen in Figs. 7 and 8 that the trajectories and Euler angle histories are smooth without any chattering, which is a common phenomenon with sliding-mode-based controllers. The use of STC with very well-tuned gains and the approximation of **sign** function in Eqn. (15) attenuated chattering almost completely. The controller implementation and RSSI measurements are carried out at an average frequency of 100 Hz. As the RSSI signals are measured in real time, a high angular resolution of $0.04°$ per measurement is achieved in the azimuthal direction.

IV. Conclusions

A UAV-based measurement methodology is proposed to measure and obtain high-resolution beam patterns for 5G AASs. The horn antenna and SDR device mounted on a UAV created experimental conditions similar to that of a typical 5G AAS beam pattern measurement. The formulation of beam pattern measurement problem into UAV path planning and trajectory tracking problems automated the measurement campaign process. Flight experiments carried out show the (a) accurate tracking performance of the designed controller and (b) satisfactory capture of antenna beam pattern. The UAV was able to complete the measurement campaign quickly and generated a high-resolution antenna pattern, validating the proposed methodology. The difference between reference antenna pattern and the measured one can be further reduced by conducting similar such low-cost UAV campaigns and averaging the result.

In the future, it is planned to extend this work and carry out the beam pattern measurement experiments outdoors on an actual 5G AAS. Several challenges arise naturally to conduct these experiments. As accurate localization of the UAV is required, RTK GPS can be used instead of a standard GPS. An automated approach can be used to speed up the application process for obtaining flight authorization. The STC designed for indoor experiments works well for one set of environmental conditions. The wind conditions, outdoors,

generate a wide range of disturbances for which one set of well-tuned gains may either cause chattering or loose sliding. In such a case, an adaptive STC can be used to automatically tune the gains during the flight.

REFERENCES

[1] K. V. Stefanik, J. C. Gassaway, K. Kochersberger, and A. L. Abbott, "Uav-based stereo vision for rapid aerial terrain mapping," *GIScience & Remote Sensing*, vol. 48, no. 1, pp. 24–49, 2011.

[2] P. Sujit, B. Hudzietz, and S. Saripalli, "Route planning for angle constrained terrain mapping using an unmanned aerial vehicle," *Journal of Intelligent & Robotic Systems*, vol. 69, pp. 273–283, 2013.

[3] M. Popović, T. Vidal-Calleja, G. Hitz, J. J. Chung, I. Sa, R. Siegwart, and J. Nieto, "An informative path planning framework for uav-based terrain monitoring," *Autonomous Robots*, vol. 44, pp. 889–911, 2020.

[4] R. Perz and K. Wronowski, "Uav application for precision agriculture," *Aircraft Engineering and Aerospace Technology*, vol. 91, no. 2, pp. 257–263, 2019.

[5] D. Erdos, A. Erdos, and S. E. Watkins, "An experimental uav system for search and rescue challenge," *IEEE Aerospace and Electronic Systems Magazine*, vol. 28, no. 5, pp. 32–37, 2013.

[6] R. Pöllänen, H. Toivonen, K. Peräjärvi, T. Karhunen, T. Ilander, J. Lehtinen, K. Rintala, T. Katajainen, J. Niemelä, and M. Juusela, "Radiation surveillance using an unmanned aerial vehicle," *Applied radiation and isotopes*, vol. 67, no. 2, pp. 340–344, 2009.

[7] D. Popescu, L. Ichim, and T. Caramihale, "Flood areas detection based on uav surveillance system," in *2015 19th International conference on system theory, control and computing (ICSTCC)*, pp. 753–758, IEEE, 2015.

[8] K. Klinkmueller, A. Wieck, J. Holt, A. Valentine, J. E. Bluman, A. Kopeikin, and E. Prosser, "Airborne delivery of unmanned aerial vehicles via joint precision airdrop systems," in *AIAA Scitech 2019 Forum*, p. 2285, 2019.

[9] M. Elloumi, R. Dhaou, B. Escrig, H. Idoudi, and L. A. Saidane, "Monitoring road traffic with a uav-based system," in *2018 IEEE wireless communications and networking conference (WCNC)*, pp. 1–6, IEEE, 2018.

[10] N. Masmoudi, W. Jaafar, S. Cherif, J. B. Abderrazak, and H. Yanikomeroglu, "Uav-based crowd surveillance in post covid-19 era," *Ieee Access*, vol. 9, pp. 162276–162290, 2021.

[11] M. Mandirola, C. Casarotti, S. Peloso, I. Lanese, E. Brunesi, and I. Senaldi, "Use of uas for damage inspection and assessment of bridge infrastructures," *International Journal of Disaster Risk Reduction*, vol. 72, p. 102824, 2022.

[12] R. Brühl, H. Fricke, and M. Schultz, "Air taxi flight performance modeling and application," in *Proceedings of the USA/Europe ATM R&D Seminar, Online*, 2021.

[13] H. Shakhatreh, A. H. Sawalmeh, A. Al-Fuqaha, Z. Dou, E. Almaita, I. Khalil, N. S. Othman, A. Khreishah, and M. Guizani, "Unmanned aerial vehicles (uavs): A survey on civil applications and key research challenges," *Ieee Access*, vol. 7, pp. 48572–48634, 2019.

[14] D. He, S. Chan, and M. Guizani, "Communication security of unmanned aerial vehicles," *IEEE Wireless Communications*, vol. 24, no. 4, pp. 134–139, 2016.

[15] M. Dai, E. Zheng, Z. Feng, L. Qi, J. Zhuang, and W. Yang, "Vision-based uav self-positioning in low-altitude urban environments," *IEEE Transactions on Image Processing*, 2023.

[16] T. M. Ghazal, "Positioning of uav base stations using 5g and beyond networks for iomt applications," 2021.

[17] H. Habibi, D. M. K. K. Venkateswara Rao, J. L. Sanchez-Lopez, and H. Voos, "On sora for high-risk uav operations under new eu regulations: Perspectives for automated approach," in *2023 International Conference on Unmanned Aircraft Systems (ICUAS)*, pp. 213–220, IEEE, 2023.

[18] V. Platzgummer, V. Raida, G. Krainz, P. Svoboda, M. Lerch, and M. Rupp, "Uav-based coverage measurement method for 5g," in *2019 IEEE 90th Vehicular Technology Conference (VTC2019-Fall)*, pp. 1–6, IEEE, 2019.

[19] F. Fuschini, M. Barbiroli, E. M. Vitucci, V. Semkin, C. Oestges, B. Strano, and V. Degli-Esposti, "An uav-based experimental setup for propagation characterization in urban environment," *IEEE Transactions on Instrumentation and Measurement*, vol. 70, pp. 1–11, 2021.

[20] V. Semkin and I. Huhtinen, "Millimeter-wave uav-based channel measurement setup," in *2021 IEEE 93rd Vehicular Technology Conference (VTC2021-Spring)*, pp. 1–2, IEEE, 2021.

[21] Z. Qiu, X. Chu, C. Calvo-Ramirez, C. Briso, X. Yin, *et al.*, "Low altitude uav air-to-ground channel measurement and modeling in semiurban environments," *Wireless Communications and Mobile Computing*, vol. 2017, 2017.

[22] L. Val-Terrón, J. J. Escudero-Garzás, L. Pérez-Roca, A. M. Vega-Viejo, and Á. Alves-González, "Air-to-ground channel characterization for unmanned aerial vehicles based on field measurements in 5g at 3.5 ghz," in *2022 18th International Conference on Wireless and Mobile Computing, Networking and Communications (WiMob)*, pp. 453–456, IEEE, 2022.

[23] B. Ning, T. Li, K. Mao, X. Chen, M. Wang, W. Zhong, and Q. Zhu, "A uav-aided channel sounder for air-to-ground channel measurements," *Physical Communication*, vol. 47, p. 101366, 2021.

[24] V. Semkin, S. Kang, J. Haarla, W. Xia, I. Huhtinen, G. Geraci, A. Lozano, G. Loianno, M. Mezzavilla, and S. Rangan, "Lightweight uav-based measurement system for air-to-ground channels at 28 ghz," in *2021 IEEE 32nd Annual International Symposium on Personal, Indoor and Mobile Radio Communications (PIMRC)*, pp. 848–853, IEEE, 2021.

[25] M. G. Fernandez, Y. A. Lopez, and F. L.-H. Andres, "On the use of unmanned aerial vehicles for antenna and coverage diagnostics in mobile networks," *IEEE Communications Magazine*, vol. 56, no. 7, pp. 72–78, 2018.

[26] M. C. Batistatos, G. E. Athanasiadou, D. A. Zarbouti, G. V. Tsoulos, and N. C. Sagias, "Lte ground-to-air measurements for uav-assisted cellular networks," 2018.

[27] S. Homayouni, M. Paier, C. Benischek, G. Pernjak, M. Leinwather, M. Reichelt, and C. Fuchsjäger, "On the feasibility of cellular-connected drones in existing 4g/5g networks: Field trials," in *2021 IEEE 4th 5G World Forum (5GWF)*, pp. 287–292, IEEE, 2021.

[28] A. Chalanga, S. Kamal, L. M. Fridman, B. Bandyopadhyay, and J. A. Moreno, "Implementation of super-twisting control: Super-twisting and higher order sliding-mode observer-based approaches," *IEEE Transactions on Industrial Electronics*, vol. 63, no. 6, pp. 3677–3685, 2016.

[29] D. M. K. K. Venkateswara Rao, H. Habibi, J. L. Sanchez-Lopez, P. P. Menon, C. Edwards, and H. Voos, "Adaptive super-twisting controller design for accurate trajectory tracking performance of unmanned aerial vehicles," *arXiv preprint arXiv:2303.11770*, 2023.

[30] Rhode&Schwartz, "R&S SMBV100B Vector Signal Generator," *Available Online: https://www.rohde-schwarz.com/nl/products/test-and-measurement/vector-signal-generators/rs-smbv100b-vector-signal-generator_63493-519808.html*, 2022.

[31] "WR-229 Standard Gain Horn Antenna Operating From 3.3 GHz to 4.9 GHz, 20 dBi Nominal Gain, Type N Female Input Connector, ProLine." http://tinyurl.com/mr2zcjyd. Accessed: 2024-02-10.

[32] Y.-N. R. Li, B. Gao, X. Zhang, and K. Huang, "Beam management in millimeter-wave communications for 5g and beyond," *IEEE Access*, vol. 8, pp. 13282–13293, 2020.

[33] "USRP B205mini-i." https://www.ettus.com/all-products/usrp-b205mini-i/. Accessed: 2024-02-10.

[34] "UHD (USRP Hardware Driver™) ." https://www.ettus.com/sdr-software/uhd-usrp-hardware-driver. Accessed: 2024-02-10.

[35] A. Zaidi, F. Athley, J. Medbo, U. Gustavsson, G. Durisi, and X. Chen, *5G Physical Layer: principles, models and technology components*. Academic Press, 2018.

[36] D. M. K. K. Venkateswara Rao and T. H. Go, "Optimization of aircraft spin recovery maneuvers," *Aerospace Science and Technology*, vol. 90, pp. 222–232, 2019.